NJC

PAPER

View Article Online
View Journal | View Issue

Cite this: *New J. Chem.*, 2021, **45**, 8032

A porphyrin-conjugated $TiO_2/CoFe_2O_4$ nanostructure photocatalyst for the selective production of aldehydes under visible light†

Mahdieh Ghobadifard,[abc] Elham Safaei,[a] Pavle V. Radovanovic[b] and Sajjad Mohebbi *[ac]

Received 27th December 2020,
Accepted 30th March 2021

DOI: 10.1039/d0nj06272c

rsc.li/njc

We investigated the photocatalytic performance of a magnetic nanohybrid of $CoFe_2O_4$ and TiO_2 heteronanostructures ($TiO_2/CoFe_2O_4$) conjugated with zinc tetrakis carboxyphenyl porphyrin (ZnTCPP) for controlled oxidation of alcohols to aldehydes under visible light. The photocatalyst was prepared by nucleating titania on pre-formed $CoFe_2O_4$ nanoparticles, generating anatase $TiO_2/CoFe_2O_4$ heteronanostructures upon annealing at 450 °C. Then, they were conjugated with ZnTCPP resulting in ZnTCPP-$TiO_2/CoFe_2O_4$ nanohybrid materials, which were characterized in detail by different structural and spectroscopic methods. The ZnTCPP-$TiO_2/CoFe_2O_4$ nanostructures have an average size of 21 nm and show ferromagnetic behavior with a magnetization saturation of 47 emu g^{-1}, a remanence of 22 emu g^{-1}, and a coercivity of *ca.* 1000 Oe. The photocatalytic conversion of alcohols up to 87% under visible light was achieved by using this hybrid nanomaterial. Such a high catalytic performance can be related to the low charge recombination rate of the ZnTCPP-$TiO_2/CoFe_2O_4$ nanostructures. The magnetic hybrid nanostructures reported in this work have excellent potential as visible light photocatalysts with advantages of high efficiency, selectivity, stability, and easy separation.

1. Introduction

Semiconductor photocatalysis has attracted much attention in environmental remediation applications due to the possibility of degrading different types of organic pollutants using only solar energy.[1] A semiconductor photocatalyst absorbs solar-radiation photons having energy equal to or larger than its bandgap energy to generate electron–hole pairs, which can then take part in the redox processes.[2] Recently, non-magnetic and magnetic particles as photocatalysts have been synthesized for use in photocatalysis applications.[3,4] Magnetic materials having specific properties have indeed been used in a range of related applications.[5–10] Specifically, $CoFe_2O_4$ with its spinel structure has attracted considerable attention for several applications such as water splitting and photodegradation of organic pollutants due to its photocatalytic activity under visible light, nontoxicity, chemical stability, low bandgap, corrosion resistance, and magnetic properties.[11] Besides, coupling $CoFe_2O_4$ with some of the wide bandgap semiconductors such as ZnO and TiO_2 has been shown to form composite photocatalysts with enhanced photocatalytic activities.[12,13] As the photocatalytic performance of TiO_2 is still rather poor owing to the fast charge recombination of exciton pairs h^+–e^-, these kinds of composite photocatalysts could speed up the rate of charge carrier separation in photocatalytic processes,[14] particularly for a TiO_2 semiconductor, due to its fine anti-photocorrosion attributes.[15]

Similar to chlorophyll in plant photosynthesis, metalloporphyrin molecules anchored to the surface of $TiO_2/CoFe_2O_4$ could act as effective sensitizers to enhance the absorption of visible light.[16] In normal photosynthesis, light absorption and excitation first occur in porphyrins. Because of the vast delocalization of π electrons, metal complexes of porphyrins have powerful absorption of light in the visible region. For dye-sensitized solar cells, among different metal porphyrin complexes, zinc tetrakis carboxyphenyl porphyrin (ZnTCPP) has been thoroughly investigated as a potential photosensitizer.[17–19] We envisaged that the modification of $TiO_2/CoFe_2O_4$ with ZnTCPP could lead to an increase in the absorption in the visible region and enhancement in the photophysical properties that could be suitable for the photo-oxidation of alcohols.[20]

In this work, the fabrication of a new three-component hybrid nanosystem composed of $CoFe_2O_4$, TiO_2, and porphyrin (Scheme 1) is reported, which allows for efficient oxidation of

[a] *Department of Chemistry, University of Kurdistan, Sanandaj, 66177-15175, Iran. E-mail: smohebbi@uok.ac.ir; Fax: +98-87-336660075; Tel: +98-87-33624133*
[b] *Department of Chemistry, University of Waterloo, 200 University Ave. W., Waterloo, ON, Canada*
[c] *Research Center for Nanotechnology, University of Kurdistan, Sanandaj, 66177-15175, Iran*

† Electronic supplementary information (ESI) available. See DOI: 10.1039/d0nj06272c

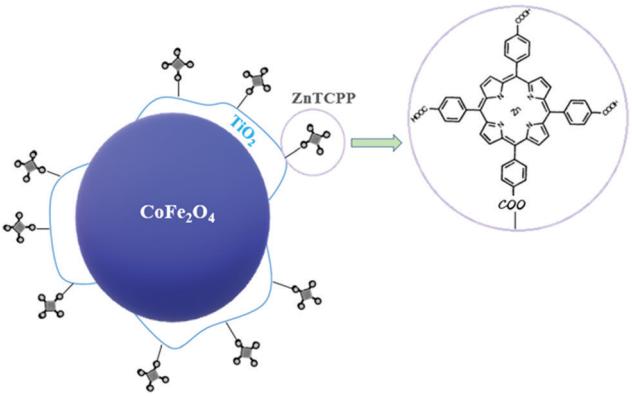

Scheme 1 Treatment of carboxyl groups of ZnTCPP and hydroxyl groups of $TiO_2/CoFe_2O_4$ nanocomposites.

alcohols using incident visible light. Furthermore, a plausible mechanism is discussed for photooxidation of alcohols using the ZnTCPP-$TiO_2/CoFe_2O_4$ nanohybrid.

2. Materials and measurements

2.1. Materials

$Fe(NO_3)_3{\cdot}9H_2O$ (99%), $Co(NO_3)_2{\cdot}6H_2O$ (99%), $Zn(CH_3COO)_2{\cdot}2H_2O$ (99%), CH_3COONa (99%), $(NH_2CH_2CH_2)_2NH$ (DETA; 98%), $Ti[OCH(CH_3)_2]_4$ (98%), methyl 4-formyl benzoate, pyrrole, $C_6H_5NO_2$, propionic acid, hydrochloric acid, ammonium oxalate (AO) and benzoquinone (BQ) were all received from Sigma-Aldrich. Dichloromethane, *t*-butyl hydroperoxide (TBHP), deionized water, absolute ethanol, and methanol were used as received. The reacting alcohols such as benzyl alcohol, 3-chlorobenzyl alcohol 98%, 4-chlorobenzyl alcohol 99%, 4-fluorobenzyl alcohol 97%, anysil alcohol (4-methoxybenzyl alcohol), and 4-nitrobenzyl alcohol with synthesis grade were purchased from Sigma-Aldrich and Merck & Co. Inc.

2.2. Preparation of $CoFe_2O_4/TiO_2$ nanostructures

The $CoFe_2O_4$ nanoparticles were synthesized as described elsewhere.[21–23] First, an aqueous solution of $C_2H_3NaO_2$ (16 g or 190 mmol in 50 mL of deionized water) was added to the mixture of Co $(NO_3)_2{\cdot}6H_2O$ (29 g, 100 mmol) and Fe $(NO_3)_3{\cdot}9H_2O$ (8 g, 20 mmol) in 50 mL of deionized water. After that, the brown color precipitate was collected using a paper filter and washed with deionized water and ethanol. The brown solid was dried in air. Finally, the $CoFe_2O_4$ nanoparticles were collected by placing the precipitate in a microwave oven (900 w) for 10 min.

The $CoFe_2O_4/TiO_2$ nanostructures were also obtained through the hydrothermal process. At first, 80 mg of $CoFe_2O_4$ nanoparticles were dispersed in 20 mL of ethanol under sonication. Then, 400 μL of $(NH_2CH_2CH_2)_2NH$ (DETA) and 22 μL of titanium(IV) isopropoxide were added to the solution. After vigorous stirring, the mixture was transferred to an autoclave and treated at a temperature of 200 °C for 20 h. After cooling down the autoclave to room temperature, the solid was separated from the solution using a magnet. The product was washed with water/ethanol several times and dried in a vacuum oven at 60 °C for 14 h. Finally, the dried product was annealed at 450 °C for 2 hours to obtain the nanostructures.

2.3. Synthesis of the ZnTCPP complex

As reported previously,[24] the desired porphyrin (H_2TCPP) was prepared by pyrrole and aromatic aldehyde. Briefly, 10 mmol of pyrrole was added dropwise to the mixture of 35 mL of propionic acid, 15 mL of nitrobenzene, and 10 mmol of benzaldehyde. After refluxing for 2 h, the mixture was solidified overnight. Finally, the purple sediment was separated by filtration and rinsed with water 5 times.

The ZnTCPP complex was prepared in a two-step process. In the first step, 0.15 mmol of zinc acetate dissolved in 5 mL of methanol was added to the solution of 100 μmol of H_2TCPP in 25 mL of CH_2Cl_2 and refluxed overnight. After the elimination of the solvent, a purple solid was obtained. In the next step, for generating porphyrin acid by the hydrolysis of porphyrin ester, 100 μmol of the purple solid in a mixture of 10 mL of tetrahydrofuran and 10 mL of ethanol (1 : 1 ratio), and 5 mL of KOH (2 M) were refluxed for 15 h. After evaporation of the solvents, the sediment was dissolved in 10 mL of water before filtering. Using hydrochloric acid (1 N), the porphyrin dipotassium salt was acidified to attain pH 2. After another filtration, the purple solid was obtained and washed with DI water.

2.4. Synthesis of the ZnTCPP-$TiO_2/CoFe_2O_4$ nanohybrid

To prepare $TiO_2/CoFe_2O_4$ nanostructures modified by ZnTCPP, 10 mL of the solution of ZnTCPP (1 mg) in methanol was added to 100 mg of suspension of $TiO_2/CoFe_2O_4$ nanostructures. The mixture was refluxed for 8 h to enable the reaction between the carboxyl groups of ZnTCPP and the hydroxyl groups on the surface of TiO_2 and link ZnTCPP on the surfaces of the nanostructures.

2.5. Measurements

The Fourier-transformed infrared (FTIR) absorption measurements were performed with a Bruker Vertex 80v spectrophotometer on the samples prepared as KBr pellets. A Mira3 Tescan field emission scanning electron microscope (FE-SEM) with energy-dispersive X-ray spectroscopy (EDS) capability was employed for large area sample imaging and elemental analysis. The powder X-ray diffraction patterns of the nanostructures were recorded using a Holland-Philips diffractometer with a Cu K_α incident radiation source (λ = 0.1542 nm) and scattering angles 2θ up to 80°. The magnetic properties of $CoFe_2O_4$, $TiO_2/CoFe_2O_4$, and ZnTCPP-$TiO_2/CoFe_2O_4$ were investigated using a vibrating sample magnetometer (VSM). The electronic absorption spectra of the nanoparticles were recorded using a Varian Cary 5000 UV-Vis-NIR spectrophotometer, and the photoluminescence (PL) spectra were recorded with a Varian Cary Eclipse fluorescence spectrometer. The X-ray photoelectron spectra (XPS) were obtained using an ESCALAB 250 spectrometer model made by VG Scientific with an Al K_α X-ray source (E_{photon} = 1486.7 eV). The transmission electron microscopy (TEM) images were obtained using a Phillips CM-10 microscope operating at 60 kV. The differential reflectance spectra (DRS) were recorded with an Avaspec-2048-TEC spectrometer.

2.6. Photocatalytic procedure

In a typical procedure, the photocatalytic reaction was carried out in a quartz cell. To control the vessel temperature during irradiation, the cell was outfitted with a water circulation system. In every run, 10 mg of the photocatalyst was added to 1.5 mL of the solvent (acetonitrile). The alcohols (referred to as a reaction substrate) and oxidant (H_2O_2) in a 1 : 15 molar ratio were then added to the cell. The mixture was placed in front of a halogen lamp at *ca.* 15 cm distance. At the end of the reaction, the photocatalyst powder was isolated using a magnet, washed with CH_3CN five times, and dried for reuse. The progress of the photoreaction was monitored by thin-layer chromatography (TLC), whereas the product was identified by gas chromatography-mass spectrometry (GC-Mass spectrophotometer).

3. Results and discussion

The absorption and photoluminescence (PL) spectra of TCPP and ZnTCPP are shown in Fig. 1. The absorption spectrum of TCPP exhibits a strong Soret band at 412 nm and four weak split Q bands at 507, 541, 584, and 640 nm. On the other hand, the absorption spectrum of ZnTCPP exhibits a strong Soret band at 421 nm and two weak split Q bands at 554 and 593 nm. The PL spectrum of TCPP has two peaks at 654 and 716 nm, while ZnTCPP exhibits two peaks at 606 and 657 nm which are similar to the literature reports for zinc porphyrin complexes.[25]

The FTIR vibration bands for $CoFe_2O_4$, $TiO_2/CoFe_2O_4$, and ZnTCPP-$TiO_2/CoFe_2O_4$ are shown in Fig. 2a–c, respectively. The band at around 470 cm^{-1} is related to the Fe(III)–O^{2-} stretching vibration of the tetrahedral metal site and the band at about 579 cm^{-1} is related to the stretching vibration in the octahedral Co(II)–O^{2-} group in $CoFe_2O_4$ (Fig. 2a).[26] The Ti–O–Ti bending or M–O stretching vibrations are associated with the peaks in the range of 800–1100 cm^{-1} (Fig. 2b).[27,28] The O–H bending mode vibrations of water may be associated with the band at 1625 cm^{-1}, and another at 3000–3600 cm^{-1} is related to the OH stretching vibration[29] (Fig. 2b). In the FT-IR spectra of ZnTCPP-$TiO_2/CoFe_2O_4$, the disappearance of N–H vibrations and the appearance of Zn–N stretching vibrations displayed at 950–1000 cm^{-1} indicate that the ZnTCPP complex was successfully synthesized.[30] The C═O and C–O stretching modes vanished, while a strong band at 1376 cm^{-1} was observed which is related to the symmetric COO stretching, suggesting that the ZnTCPP was immobilized on the surface of $TiO_2/CoFe_2O_4$ through the carboxylic acid groups.[31,32] The pyrrole stretching vibration bands appear at about 1650 cm^{-1} for C═N bonds (Fig. 2c). The bands at 2800–2900 cm^{-1} correspond to the symmetric C–H stretching mode of the CH_2. The bridge bonding between $TiO_2/CoFe_2O_4$ and ZnTCPP provides a path for effective transmission of electrons from the $TiO_2/CoFe_2O_4$ to the HOMO level of ZnTCPP, which can be used effectively for photoreactions.

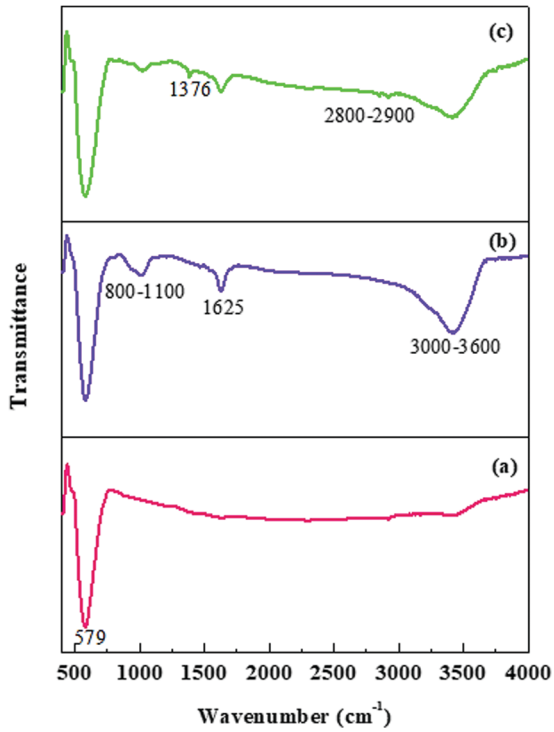

Fig. 2 FT-IR spectra of (a) $CoFe_2O_4$, (b) $TiO_2/CoFe_2O_4$, and (c) ZnTCPP-$TiO_2/CoFe_2O_4$ nanohybrids.

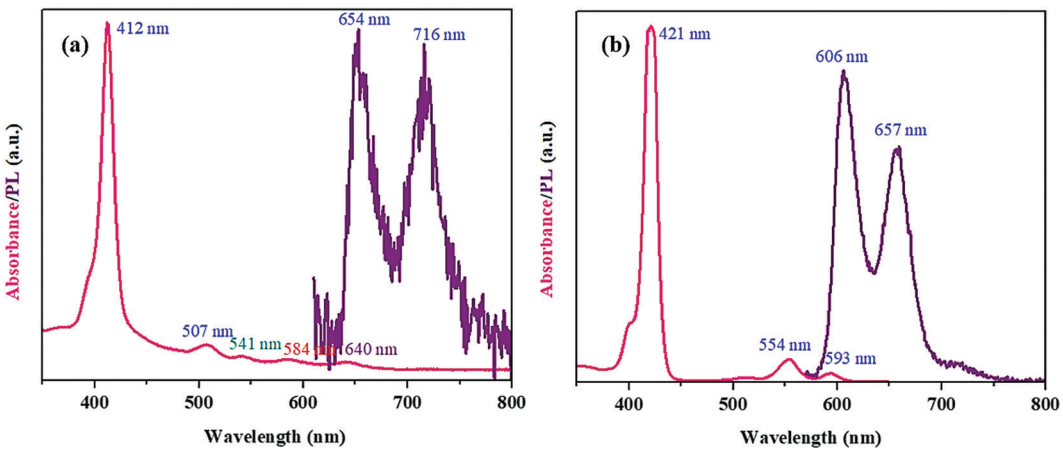

Fig. 1 The absorption and PL spectra of (a) TCPP and (b) ZnTCPP at room temperature.

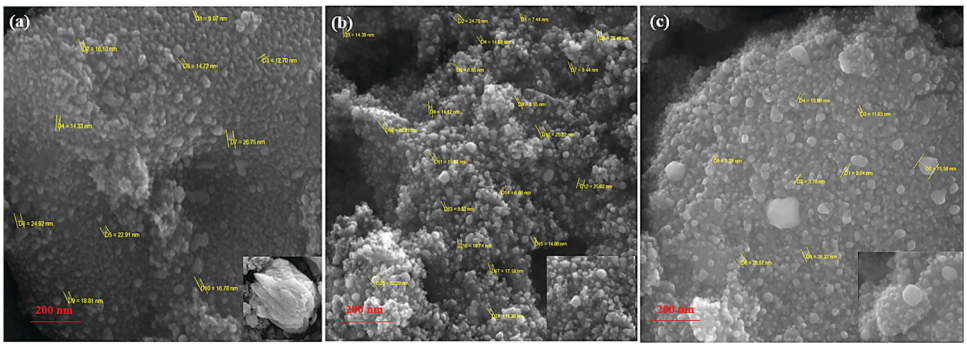

Fig. 3 SEM images of (a) $CoFe_2O_4$, (b) $TiO_2/CoFe_2O_4$, and (c) ZnTCPP-$TiO_2/CoFe_2O_4$ nanohybrids.

Due to the low loading of the porphyrin complex on the surfaces of the nanostructures, these peaks have very low intensities. In other words, the intensity of the peaks reflects the amount of organic materials on the surfaces of inorganic materials.

The FESEM images of $CoFe_2O_4$, TiO_2@$CoFe_2O_4$, and ZnTCPP-$TiO_2/CoFe_2O_4$ particles are shown in Fig. 3. The $CoFe_2O_4$ particles adopt a flower-like morphology through the junction of nanosheets, while TiO_2 is deposited on the surface of the $CoFe_2O_4$ nanoparticles to form hybrid $TiO_2/CoFe_2O_4$ nanostructures. The SEM image of ZnTCPP-$TiO_2/CoFe_2O_4$ in Fig. 3c demonstrates that the sample consists of relatively uniform microparticles. The average sizes of $CoFe_2O_4$, $TiO_2/CoFe_2O_4$, and ZnTCPP-$TiO_2/CoFe_2O_4$ particles are *ca.* 17, 16, and 21 nm, respectively. Herein, this small decrease of average size (about 1 nm) is due to the use of the microwave method for obtaining $CoFe_2O_4$ instead of the sol–gel method. The $CoFe_2O_4$ was prepared under microwave irradiation using a heterometallic oxo-centered trinuclear $[CoFe_2O(CH_3COO)_6(H_2O)_3]\cdot 2H_2O$ complex as a precursor with an average size of 17 nm, while $TiO_2/CoFe_2O_4$ was prepared by the sol–gel method. This method makes it fully dissolved and the size decreased.

The elemental composition of $CoFe_2O_4$, $TiO_2/CoFe_2O_4$, and ZnTCPP-$TiO_2/CoFe_2O_4$ nanostructures was confirmed by EDS analysis (Fig. 4). Co, Fe, and O were found in all samples. Additionally, Ti was present in the $TiO_2/CoFe_2O_4$ nanoparticles, and Ti, N, Zn, and C in the ZnTCPP-$TiO_2/CoFe_2O_4$ nanostructures. The molar ratio of Co/Fe was 1 : 1.96 for the $CoFe_2O_4$

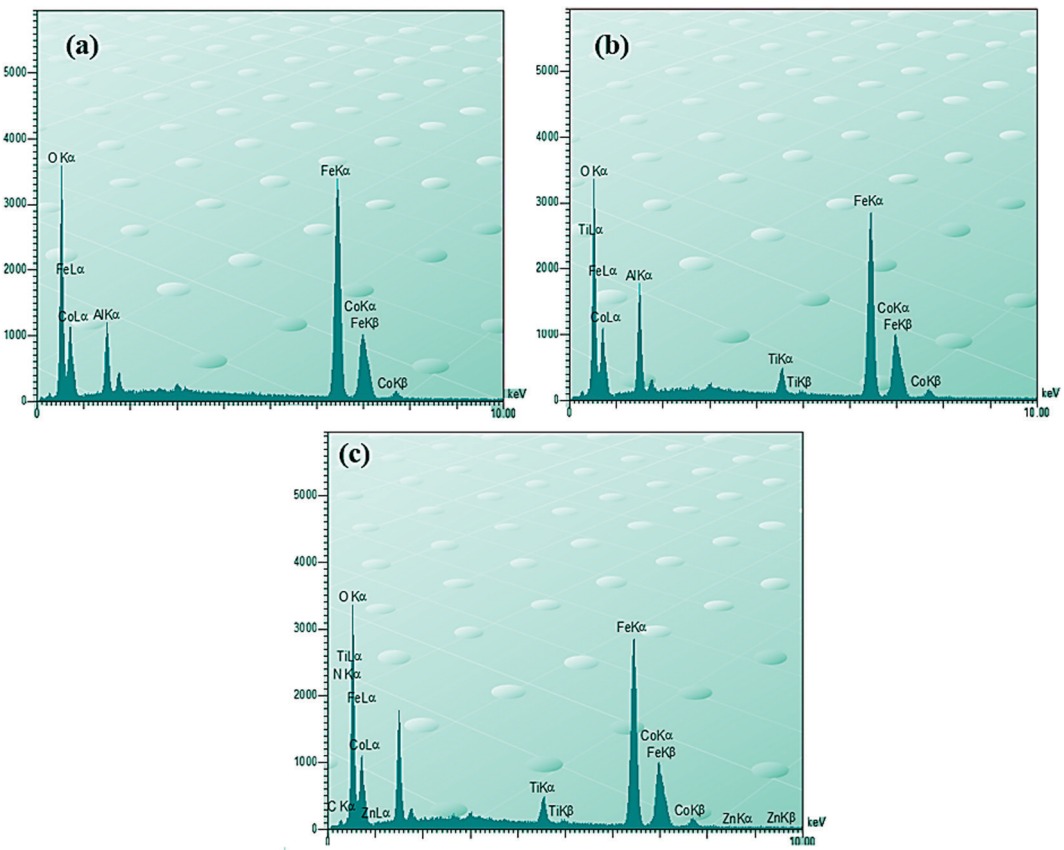

Fig. 4 EDS spectra of (a) $CoFe_2O_4$, (b) $TiO_2/CoFe_2O_4$, and (c) ZnTCPP-$TiO_2/CoFe_2O_4$ nanohybrids.

nanoparticles, 1 : 1.71 for the $TiO_2/CoFe_2O_4$ nanoparticles, and 1 : 1.62 for the ZnTCPP-$TiO_2/CoFe_2O_4$ hybrid nanostructures (Fig. 4). This result affirms that the core components of $CoFe_2O_4$, $TiO_2/CoFe_2O_4$, and ZnTCPP-$TiO_2/CoFe_2O_4$ remain constant.

The morphologies of cobalt ferrite nanoparticles, cobalt ferrite nanoparticles modified with TiO_2, and ZnTCPP-$TiO_2/CoFe_2O_4$ hybrid nanostructures were characterized by TEM and show a reasonably uniform size distribution. The $CoFe_2O_4$ nanoparticles consist of stacked nanosheets (Fig. 5a), while the $TiO_2/CoFe_2O_4$ nanoparticles have irregular morphologies, for which the darker areas are due to $CoFe_2O_4$ and the lighter areas correspond to TiO_2, suggesting the interface formation between TiO_2 and $CoFe_2O_4$ (Fig. 5b and c). No change in the morphology of the $TiO_2/CoFe_2O_4$ nanoparticles was observed from the TEM image after combining with ZnTCPP (Fig. 5d).

The XRD patterns of the $CoFe_2O_4$, $TiO_2/CoFe_2O_4$, and ZnTCPP-$TiO_2/CoFe_2O_4$ nanostructures confirm their crystal structures, as shown in Fig. 6. In the XRD pattern of the $CoFe_2O_4$ nanoparticles (Fig. 6a), the reflection plains (111), (220), (311), (222), (400), (422), (511), (440), (531) and (620) match that of JCPDS No. 22-1086, as expected. The XRD pattern of the $TiO_2/CoFe_2O_4$ sample is shown in Fig. 6b. These samples were prepared by a hydrothermal method and subsequently annealed at 450 °C. The transformation of the anatase to rutile phase occurs at an annealing temperature $T > 600$ °C. The diffraction peaks in Fig. 6b correspond to the (101), (004), (200), (105), and (204) planes of anatase TiO_2 and are ascribed to the presence of anatase TiO_2 in the samples (JCPDS No. 21-1272).[33] Due to the larger amount of $CoFe_2O_4$ in the sample, its peak intensity is higher than that of TiO_2. Fig. 6c shows the XRD pattern of the ZnTCPP-$TiO_2/CoFe_2O_4$ hybrid nanostructures, which is very similar to that of the $TiO_2/CoFe_2O_4$ hetero-nanostructures. Thus, the $TiO_2/CoFe_2O_4$ particles have a robust structure that remained stable during sample processing.

The magnetic hysteresis loops for the $CoFe_2O_4$, $TiO_2/CoFe_2O_4$, and ZnTCPP-$TiO_2/CoFe_2O_4$ samples were measured at room temperature (Fig. 7). Owing to the presence of the $CoFe_2O_4$ nanoparticles, the samples behave as a soft ferromagnet, with saturation magnetization (M_s) values of 56.99, 51.77, and 47.02 emu g^{-1} for $CoFe_2O_4$, $TiO_2/CoFe_2O_4$, and ZnTCPP-$TiO_2/CoFe_2O_4$, respectively. The saturation magnetization of the $CoFe_2O_4$ particles is higher than that of the $TiO_2/CoFe_2O_4$ and ZnTCPP-$TiO_2/CoFe_2O_4$ particles, showing the possibility of ZnTCPP-$TiO_2/CoFe_2O_4$ having a M_r value less than that in pure $CoFe_2O_4$.[34] When $CoFe_2O_4$ was combined with TiO_2 and ZnTCPP, the magnetic moments in TiO_2 and ZnTCPP may be caused owing to the magnetic proximity effect and high ferromagnetic properties.[35] The corresponding values of remnant

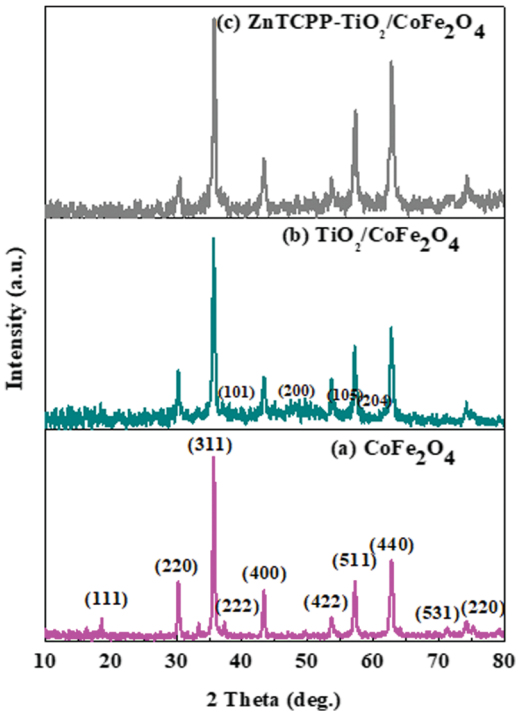

Fig. 6 The powder XRD patterns of (a) $CoFe_2O_4$ nanoparticles, (b) $TiO_2/CoFe_2O_4$ hetero-nanostructures, and (c) ZnTCPP-$TiO_2/CoFe_2O_4$ nanohybrid.

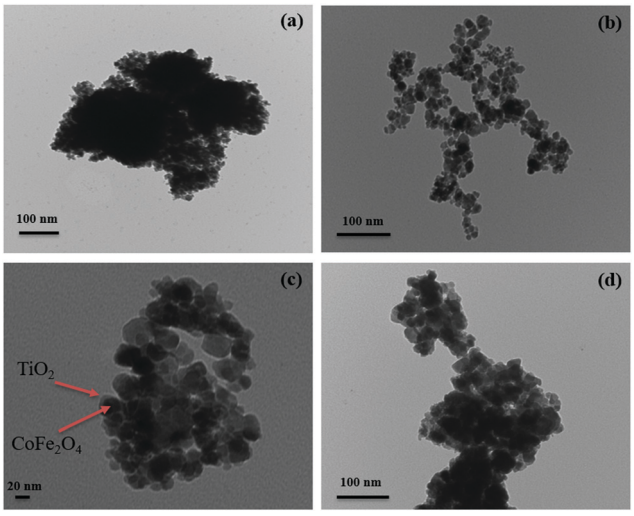

Fig. 5 The TEM images of nanoparticles: (a) $CoFe_2O_4$, (b and c) $TiO_2/CoFe_2O_4$, and (d) ZnTCPP-$TiO_2/CoFe_2O_4$ nanohybrids.

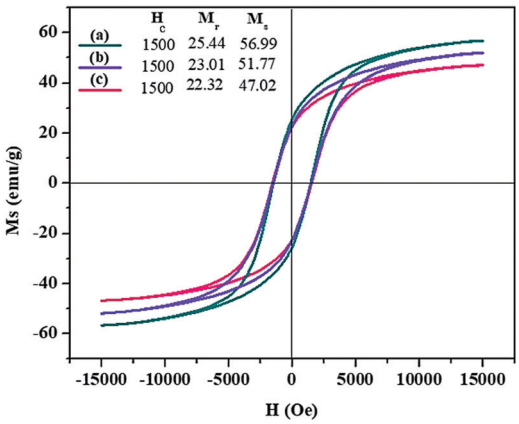

Fig. 7 The room temperature field-dependent magnetization curves of the (a) $CoFe_2O_4$ nanoparticles, (b) $TiO_2/CoFe_2O_4$ hetero-nanostructures, and (c) ZnTCPP-$TiO_2/CoFe_2O_4$ nanohybrids.

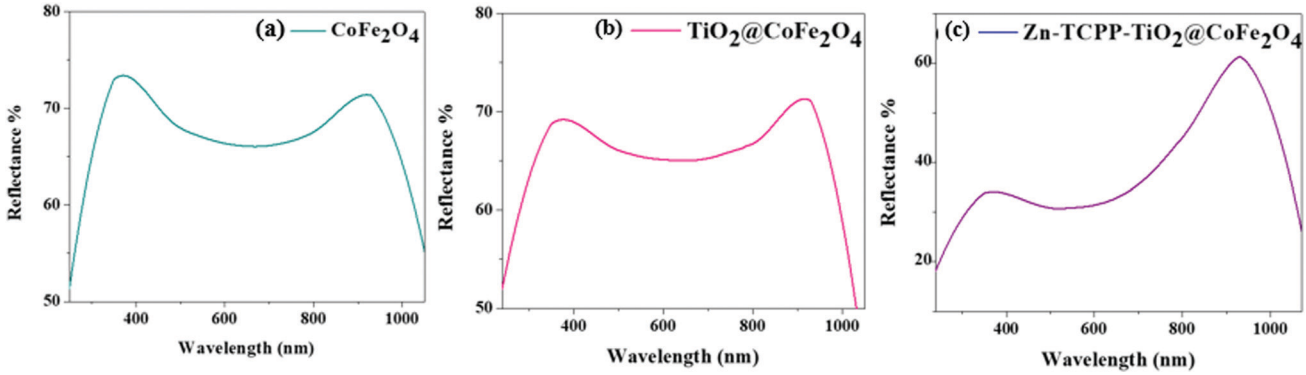

Fig. 8 The UV-vis DRS analysis curves of the (a) $CoFe_2O_4$, (b) $TiO_2/CoFe_2O_4$, and (c) ZnTCPP-$TiO_2/CoFe_2O_4$ nanohybrids.

magnetization, M_r, are 25.44, 23.01, and 22.32 emu g^{-1}, with a coercive field (H_c) of *ca.* 1500 Oe. Finally, the ferromagnetic properties of the as-prepared ZnTCPP-$TiO_2/CoFe_2O_4$ nanostructures imply that this hybrid is easily recovered from the solution mixture using a permanent magnet after a photocatalytic reaction. So, the overall photocatalytic performance improved due to easy separation, washing, and reusing of the catalyst.

The DRS measurements and analyses were performed to investigate the absorption of the $CoFe_2O_4$, $TiO_2/CoFe_2O_4$, and ZnTCPP-$TiO_2/CoFe_2O_4$ powder nanostructures (Fig. 8). The $CoFe_2O_4$ nanoparticles have relatively small bandgap energy (1.24 eV), while the absorption onset for the ZnTCPP-$TiO_2/CoFe_2O_4$ nanostructures is 1.41 eV (Fig. 1S, ESI†). As a result, the ZnTCPP-$TiO_2/CoFe_2O_4$ nanohybrid has potential to exhibit considerable photocatalytic activity under visible light by readily generating electron–hole pairs. Also, Fig. 9 shows the electronic absorption spectra of the $TiO_2/CoFe_2O_4$ and ZnTCPP-$TiO_2/CoFe_2O_4$ powder nanostructures.

The chemical states and elemental composition of the ZnTCPP-$TiO_2/CoFe_2O_4$ hybrid nanostructures were determined by XPS analysis. A set of characteristic XPS peaks for Zn, Co, Fe, O, Ti, N, and C are observed in the survey scan of the ZnTCPP-$TiO_2/CoFe_2O_4$ nanohybrid (Fig. 10a). The XPS signal for C 1s consists of three asymmetric peaks at 285.4, 286.5, and 289.2 eV

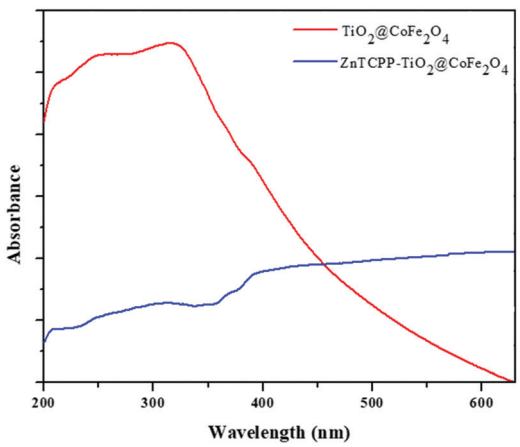

Fig. 9 The electronic absorption spectra of the $TiO_2/CoFe_2O_4$ and ZnTCPP-$TiO_2/CoFe_2O_4$ nanohybrids.

corresponding to the C–C and C═C bonds of the TCPP ring, and the carbonyl of the –COO group, respectively (Fig. 10b).[36] The O 1s spectrum displays spectral features at 530.4, 531.8, and 533.5 eV that can be assigned to the metal–oxygen–metal (M–O–M) bridge in TiO_2 and/or $CoFe_2O_4$, oxygen in the terminal –OH bonds (Ti–OH), and oxygen defects in TiO_2, respectively (Fig. 10c).[37,38] This oxygen deficiency should be attributed to Ti^{3+} which is formed during synthesis and may not contribute to free carbon. The Ti 2p spectrum exhibits two peaks for Ti^{4+} in TiO_2 at 458.9 and 464.8 eV due to the $2p_{3/2}$ and $2p_{1/2}$ states, respectively (Fig. 10d).[39] The peak appearing at 460.3 eV corresponds to Ti^{3+} in Ti_2O_3.[40] Both Ti^{4+} and Ti^{3+} on the surface of TiO_2 demonstrate that during the solvothermal reactions, numerous oxygen vacancies are formed.[41] So, the Ti^{3+} with a lower oxidation state confirms the oxygen deficiency which is required for charge balance.[42] The existing Ti^{3+} species increase the photocatalytic activity through the creation of new mid-gap states. These states have two functions: (i) redshift the absorption and (ii) function as electron traps that prevent electron–hole pair recombination. Under visible light irradiation, electrons can be excited to Ti^{3+} and V_O impurity levels with a longer lifetime than the lifetime of the photogenerated electrons in the CB[43] which could be confirmed by a jump in PL at 585 nm (Fig. 11). The mid-gap states originating from Ti^{3+} greatly suppress the charge carrier recombination rate that provides feasibility for electron transfer.[44]

The photoluminescence spectra of the $TiO_2/CoFe_2O_4$ and ZnTCPP-$TiO_2/CoFe_2O_4$ nanostructures are shown in Fig. 11. The higher intensity signal of $TiO_2/CoFe_2O_4$ indicates higher charge recombination relative to the ZnTCPP-$TiO_2/CoFe_2O_4$ hybrid nanostructures. By loading ZnTCPP on the surfaces of the $TiO_2/CoFe_2O_4$ nanoparticles, the electron transfer could be improved along with the reduction in charge recombination. The lower PL intensity suggests a lower charge recombination rate, owing to the efficient charge carrier separation, which can, in turn, stimulate the photocatalytic activity.[21] The PL intensity of the ZnTCPP-$TiO_2/CoFe_2O_4$ sample was negligible, suggesting that the charge recombination is significantly decreased. As shown in Fig. 11, the PL line of Zn-TCPP-$TiO_2/CoFe_2O_4$ has not jumped at about 558 nm while this small jump or namely one weak peak was observed for $TiO_2/CoFe_2O_4$ that could be attributed to the existence of a mid-state energy level.

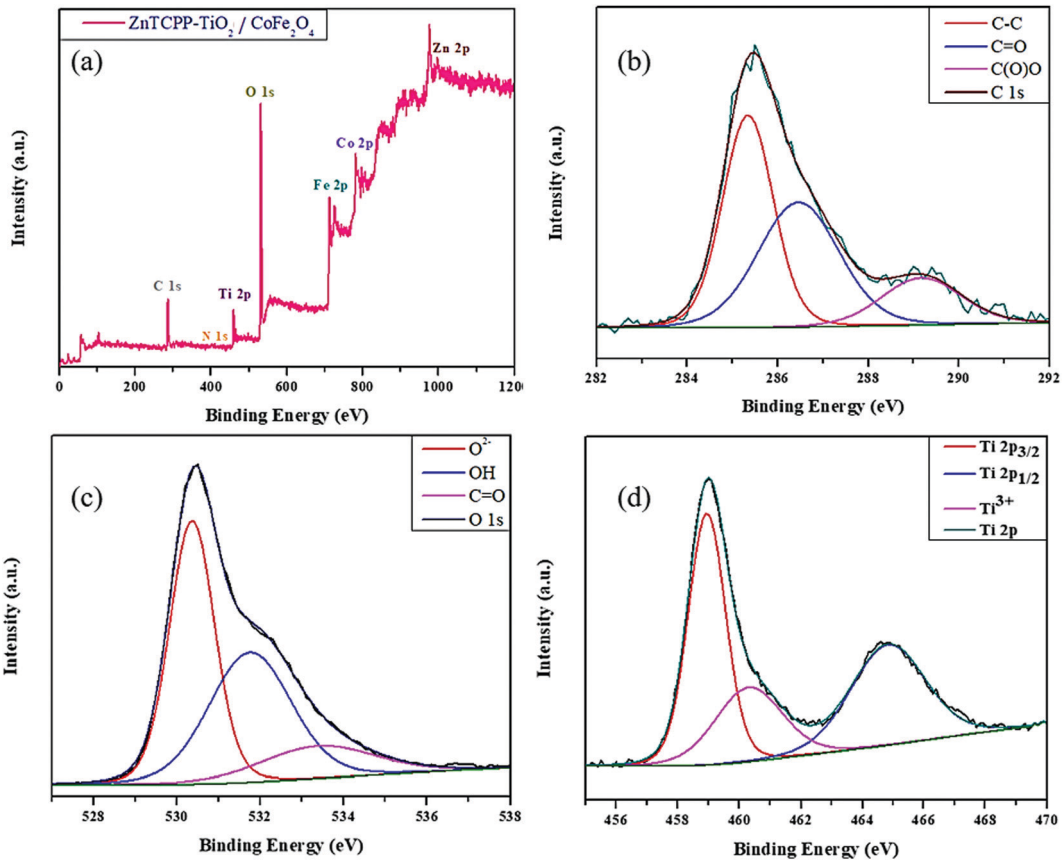

Fig. 10 (a) XPS spectrum of the ZnTCPP-TiO_2/$CoFe_2O_4$ nanohybrid, and (b–d) characteristic high-resolution XPS peaks: (b) C 1s, (c) O 1s, and (d) Ti 2p.

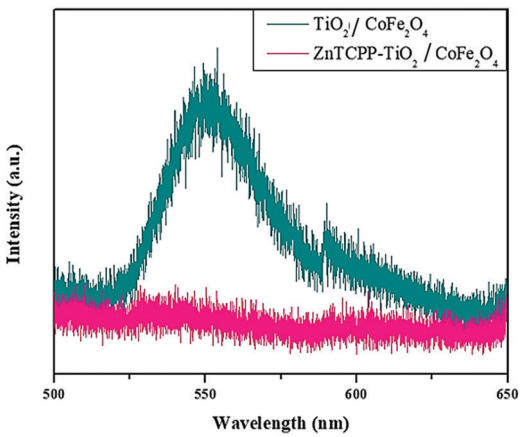

Fig. 11 PL spectra of the as-prepared TiO_2/$CoFe_2O_4$ hetero-nanostructures and ZnTCPP-TiO_2/$CoFe_2O_4$ hybrid nanostructures. The spectra were collected for the excitation wavelength of 350 nm.

4. Photocatalytic oxidation of primary alcohols

As revealed by different analyses, the ZnTCPP-TiO_2/$CoFe_2O_4$ nanohybrid is a promising candidate for controlled photocatalytic oxidation of alcohols to aldehydes in the visible region of electromagnetic irradiation. The optimized conditions for the photocatalytic reaction were identified by performing initial photocatalytic reactions (Table 1). In a pyrex cell, different amounts of the photocatalyst and 100 μmol of benzyl alcohol, used as a substrate, were mixed. For photo-oxidation of alcohols, the catalyst dosage under visible light irradiation was optimized. The oxidation efficiency depends on the catalyst amount. The oxidation yield was enhanced by increasing the catalyst amount up to 10 mg, but a higher amount of catalyst from 10 to 15 mg leads to a decline in the oxidation performance (Table 1). This occurrence might be related to the aggregation of particles and loss of active areas on the surface of the catalyst.[45] The oxidation reaction was negligible in the dark or in the absence of a catalyst (Table 1, entries 13 and 14). It was corroborated that the reaction does not occur with a ZnTCPP-TiO_2/$CoFe_2O_4$ nanohybrid without irradiation. Likewise, the reaction did not proceed without a ZnTCPP-TiO_2/$CoFe_2O_4$ nanohybrid. Therefore, both the ZnTCPP-TiO_2/$CoFe_2O_4$ nanohybrid and light irradiation are essential for catalyzing the oxidation reaction.

4.1. Effect of different solvents on the catalytic reaction

We used the optimized conditions to study the efficacy of solvent polarity on the efficacy of the oxidation reaction. For this reaction, 100 μmol of benzyl alcohol and 10 mg of the photocatalyst were mixed in different solvents, including CH_3CN, CH_2Cl_2, C_3H_7NO, $CHCl_3$, and H_2O. The solvents have a significant effect on the photocatalytic efficiency of hybrid nanostructures *via* energy transfer, particle polarization, and scattering.[46] Acetonitrile showed the

Table 1 Optimization of photocatalytic oxidation conditions for benzyl alcohol to aldehyde under visible light irradiation[a]

Entry	Photocatalyst	Photocatalyst (mg)	Product	Selectivity%	Conversion%
1	$CoFe_2O_4$	5	Benzaldehyde	>99	14
2	$TiO_2/CoFe_2O_4$	5	Benzaldehyde	>99	30
3	ZnTCPP-$TiO_2/CoFe_2O_4$	5	Benzaldehyde	>99	53
4	$CoFe_2O_4$	8	Benzaldehyde	>99	32
5	$TiO_2/CoFe_2O_4$	8	Benzaldehyde	>99	53
6	ZnTCPP-$TiO_2/CoFe_2O_4$	8	Benzaldehyde	>99	79
7	$CoFe_2O_4$	10	Benzaldehyde	>99	39
8	$TiO_2/CoFe_2O_4$	10	Benzaldehyde	>99	61
9	ZnTCPP-$TiO_2/CoFe_2O_4$	10	Benzaldehyde	>99	87
10	$CoFe_2O_4$	15	Benzaldehyde	>99	33
11	$TiO_2/CoFe_2O_4$	15	Benzaldehyde	>99	58
12	ZnTCPP-$TiO_2/CoFe_2O_4$	15	Benzaldehyde	>99	82
13	No Catalyst	0	Benzaldehyde	—	<1
14	ZnTCPP-$TiO_2/CoFe_2O_4$(no light irradiation)	10	Benzaldehyde	—	<1

[a] H_2O_2, 1.5 mmol and reaction time, 120 min. Conversion percentage on the basis of benzyl alcohol consumption $(\Delta C/C_0) \times 100$.

Table 2 The efficacy of solvents in the photo-oxidation of benzyl alcohol under optimized conditions[a]

Entry	Photocatalyst	Time (min)	Solvent	Selectivity%	Conversion%
1	$CoFe_2O_4$	120	CH_3CN	>99	39
2	$TiO_2/CoFe_2O_4$	120	CH_3CN	>99	61
3	ZnTCPP-$TiO_2/CoFe_2O_4$	120	CH_3CN	>99	87
4	$CoFe_2O_4$	120	CH_2Cl_2	>99	27
5	$TiO_2/CoFe_2O_4$	120	CH_2Cl_2	>99	38
6	ZnTCPP-$TiO_2/CoFe_2O_4$	120	CH_2Cl_2	>99	62
7	$CoFe_2O_4$	120	C_3H_7NO	—	—
8	$TiO_2/CoFe_2O_4$	120	C_3H_7NO	—	—
9	ZnTCPP-$TiO_2/CoFe_2O_4$	120	C_3H_7NO	>99	<4
10	$CoFe_2O_4$	120	$CHCl_3$	>99	32
11	$TiO_2/CoFe_2O_4$	120	$CHCl_3$	>99	40
12	ZnTCPP-$TiO_2/CoFe_2O_4$	120	$CHCl_3$	>99	73
13	$CoFe_2O_4$	120	H_2O	—	—
14	$TiO_2/CoFe_2O_4$	120	H_2O	—	—
15	ZnTCPP-$TiO_2/CoFe_2O_4$	120	H_2O	>99	<6

[a] H_2O_2 1.5 mmol.

highest conversion percentage of the oxidation of benzyl alcohol, while water displayed the minimum yield (Table 2). The selectivity generally remained more than 99% with aldehyde as the only product.

The photocatalytic activity of the $CoFe_2O_4$, $TiO_2/CoFe_2O_4$, and ZnTCPP-$TiO_2/CoFe_2O_4$ nanostructures for the oxidation of various alcohol derivatives is shown in Table 3. The oxidation of alcohol was achieved with >99% selectivity. The $CoFe_2O_4$ nanoparticles show poor photoactivity as reflected through the lower yield of alcohol conversion compared to the $TiO_2/CoFe_2O_4$ hetero-nanostructures and ZnTCPP-$TiO_2/CoFe_2O_4$ nanohybrids, which is sensible given their insignificant visible light absorptivity. On the other hand, the ZnTCPP-$TiO_2/CoFe_2O_4$ nanostructures exhibited higher activity than the $TiO_2/CoFe_2O_4$ nanoparticles due to the decreased charge recombination in the nanohybrid and the powerful absorption of the porphyrin complex in the visible region due to the significant delocalization of π electrons. This processing could be generalized for various aromatic alcohols containing both electron-withdrawing and electron-donating groups. The rates of reactions of substituted benzyl alcohol depend on their electronic character which is higher for electron-withdrawing substituents compared to electron-donating ones.

To achieve the optimal reaction conditions, various factors which affect the progress of the reaction, including the amount of catalyst, solvent polarity, and oxidants, were considered. According to the test results, the optimized conditions for the photocatalytic reaction are 10 mg of the catalyst and acetonitrile as the solvent. As seen in Table 4, *tert*-butyl hydroperoxide (TBHP) shows the highest conversion percentage compared to other oxidants, such as H_2O_2 or O_2. TBHP, as most hydroperoxides, is completely reactive with most polymers, metals, bases, and acids. TBHP forms a more stable radical species than the related H_2O_2 homolog. However, TBHP is a more "huge" substrate (due to the *tert*-butyl side chain) than H_2O_2. It displays some differences in the substrate reactivity to certain types of catalysts. Despite higher catalytic performance in the presence of TBHP, H_2O_2 was used as an oxidant, due to several advantages such as being inexpensive, ecofriendly, safer, and milder.

4.2. Plausible photocatalytic mechanisms

The active species and/or intermediates in alcohol oxidation reactions using ZnTCPP-$TiO_2/CoFe_2O_4$ hybrid nanostructures as the catalyst were investigated by using sacrificial trapping reagents under optimized conditions (Fig. 12). In the trapping experiment, a radical scavenger TBHP was chosen for the detection of hydroxyl radicals, AO for the detection of holes, and BQ for superoxide radicals.[47,48] In the presence of TBHP, 94% of benzyl alcohol was oxidized under visible light and optimized conditions, while in the presence of AO and BQ, only 17% and <5% of benzyl alcohol were oxidized, respectively. Therefore, superoxide radicals are not the active species for the ZnTCPP-$TiO_2/CoFe_2O_4$ nanohybrid as the

Table 3 The selective photooxidation of substituted alcohols using $CoFe_2O_4$, $TiO_2/CoFe_2O_4$, and ZnTCPP-$TiO_2/CoFe_2O_4$ under visible light[a]

Ingress	Catalyst	Substrate	Product	Y%	S%
1	$CoFe_2O_4$	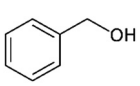	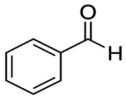	39	>99
2	$TiO_2/CoFe_2O_4$			61	>99
3	ZnTCPP-$TiO_2/CoFe_2O_4$			87	>99
4	$CoFe_2O_4$	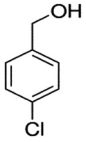	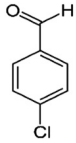	28	>99
5	$TiO_2/CoFe_2O_4$			43	>99
6	ZnTCPP-$TiO_2/CoFe_2O_4$			65	>99
7	$CoFe_2O_4$	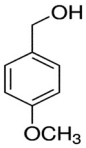	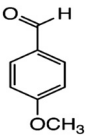	19	>99
8	$TiO_2/CoFe_2O_4$			34	>99
9	ZnTCPP-$TiO_2/CoFe_2O_4$			43	>99
10	$CoFe_2O_4$	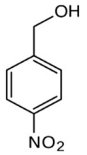	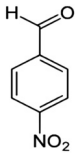	2	>99
11	$TiO_2/CoFe_2O_4$			5	>99
12	ZnTCPP-$TiO_2/CoFe_2O_4$			26	>99
13	$CoFe_2O_4$	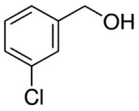	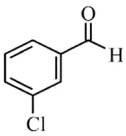	36	>99
14	$TiO_2/CoFe_2O_4$			56	>99
15	ZnTCPP-$TiO_2/CoFe_2O_4$			68	>99
16	$CoFe_2O_4$	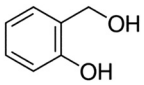	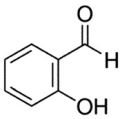	8	>99
17	$TiO_2/CoFe_2O_4$			19	>99
18	ZnTCPP-$TiO_2/CoFe_2O_4$			45	>99
19	$CoFe_2O_4$	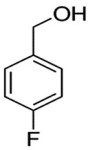	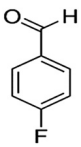	33	>99
20	$TiO_2/CoFe_2O_4$			45	>99
21	ZnTCPP-$TiO_2/CoFe_2O_4$			81	>99

[a] H_2O_2 1.5 mmol, reaction time 120 min.

Table 4 The efficacy of various oxidants on the photo-oxidation reaction of benzyl alcohol[a]

Ingress	Catalyst	Solvent	Oxidant	Selectivity%	Yield%
1	$CoFe_2O_4$	CH_3CN	TBHP	>99	40
2	$TiO_2/CoFe_2O_4$	CH_3CN	TBHP	>99	63
3	ZnTCPP-$TiO_2/CoFe_2O_4$	CH_3CN	TBHP	>99	94
4	$CoFe_2O_4$	CH_3CN	H_2O_2	>99	39
5	$TiO_2/CoFe_2O_4$	CH_3CN	H_2O_2	>99	61
6	ZnTCPP-$TiO_2/CoFe_2O_4$	CH_3CN	H_2O_2	>99	87
7	$CoFe_2O_4$	CH_3CN	O_2	—	—
8	$TiO_2/CoFe_2O_4$	CH_3CN	O_2	—	—
9	ZnTCPP-$TiO_2/CoFe_2O_4$	CH_3CN	O_2	>99	<5

[a] H_2O_2, 1.5 mmol and reaction time, 120 min.

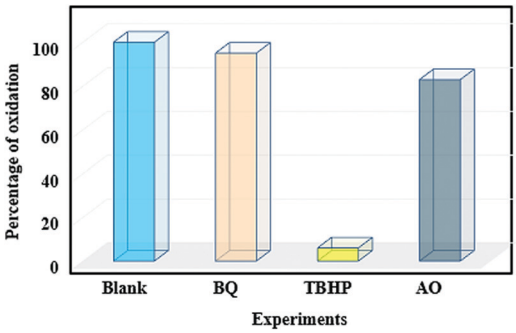

Fig. 12 Effects of the trapping agents on the photocatalytic oxidation of alcohols with the ZnTCPP-$TiO_2/CoFe_2O_4$ nanohybrid under incident visible light using *t*-butyl hydroperoxide (TBHP), ammonium oxalate (AO), and benzoquinone (BQ).

photocatalyst, while h^+ and $^{\circ}OH$ appear to be the main active species for this reaction.

The schematics of the mechanism of the photocatalytic oxidation of alcohols using the ZnTCPP-$TiO_2/CoFe_2O_4$ hybrid nanosystem are demonstrated in Fig. 13. The increased photoactivity of this nanohybrid can be ascribed to the fast charge transfer processes.[49,50] Upon irradiation with visible light, the electron–hole pairs are generated in $CoFe_2O_4$ and TiO_2 due to electron excitation from the VB to CB. Although TiO_2 is a wide bandgap n-type semiconductor, a redshift of the absorbed light to the visible area is observed. This redshift is due to the creation of Ti^{3+}-derived mid-gap states as a result of oxygen deficiency.[51] These mid-gap states originating from Ti^{3+} greatly suppress the charge carrier recombination rate that provides feasibility for electron transfer.[44] Conversely, $CoFe_2O_4$ is a p-type semiconductor.[52] Thus, these two components could form a p–n junction. The $TiO_2/CoFe_2O_4$ hetero-nanostructure is further functionalized with ZnTCPP, which acts as an excellent sensitizer and improves the photocatalytic performance of the ZnTCPP-$TiO_2/CoFe_2O_4$ nanohybrid in the visible light region. The CB and VB positions of the semiconductors were calculated using the following equations:[53,54]

$$E_{VB} = \chi - E_e + 0.5E_g \quad (1)$$

$$E_{CB} = E_{VB} - E_g \quad (2)$$

where E_{VB} and E_{CB} are the potential energy levels of the valence band and conduction band, respectively, E_g is the bandgap energy, E_e is the hydrogen-scale free electron energy, and χ is the electronegativity of $CoFe_2O_4$ or TiO_2. Based on the values of E_g for $CoFe_2O_4$ and TiO_2 which are 1.24 eV (Fig. 8b) and 3.20 eV,[22,55] respectively, the E_{VB} and E_{CB} for both of them were calculated by eqn (1) and (2) (Table 5).

The oxidation potential ($E_{S^+/S^{\circ}}$) of the excited dye is −1.00 eV, which is more negative than the CB of TiO_2, and the oxidized ZnTCPP dye shows a positive oxidation potential ($E_{S^+/S}$), +1.23 eV.[20] In the p-type $CoFe_2O_4$, the Fermi level (E_F) is above E_{VB}, while in the n-type TiO_2, it is below E_{CB}.[57] Before contact, the E_{CB} and E_F levels of $CoFe_2O_4$ are lower than those of TiO_2,

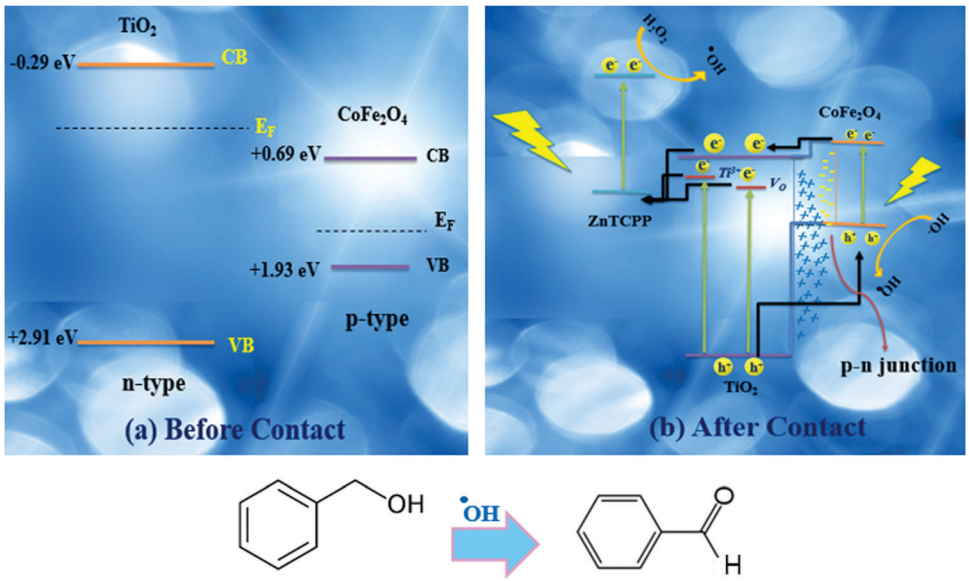

Fig. 13 A plausible mechanism of the photoactivity of the ZnTCPP-TiO_2/$CoFe_2O_4$ nanohybrid in the visible region.

Table 5 The values of χ,[56] E_g, E_{CB}, and E_{VB} parameters of the semiconductors in eV[a]

Semiconductors	χ	E_g	E_{CB}	E_{VB}
$CoFe_2O_4$	5.81	1.24	+0.69	+1.93
TiO_2	5.81	3.20	−0.29	+2.91

[a] Hydrogen-scale free electron energy of 4.5 eV is considered.

as illustrated in Fig. 13a. After the two materials come into contact, the E_F level of TiO_2 decreases while the E_F level of $CoFe_2O_4$ increases. The electron transfer from TiO_2 to $CoFe_2O_4$ across the p–n junction continues until equilibrium is reached at the interface, which results in the formation of the space-charge area. All energy levels of TiO_2 descend, while those of $CoFe_2O_4$ rise.[58,59] Therefore, the CB of TiO_2 is lower than the CB of $CoFe_2O_4$, and upon excitation, under visible light, the electrons move from the CB of $CoFe_2O_4$ to the CB of TiO_2. According to previous reports,[60,61] below the CB of TiO_2, the mid-state energy levels correspond to Ti^{3+} and V_O, which causes a decrease in the apparent optical E_g of TiO_2. Under visible light irradiation, electrons can be excited to Ti^{3+} and V_O impurity levels with a longer lifetime than the lifetime of the photogenerated electrons in the CB.[43] The mid-gap states originating from Ti^{3+} greatly suppress the charge carrier recombination rate that provides feasibility for electron transfer.[44] Electrons in the CB of TiO_2 and defect sites (Ti^{3+} and V_O) are transferred to the oxidized levels of the ZnTCPP dye; these electrons are then excited from the HOMO to the LUMO orbital of ZnTCPP to reduce H_2O_2 to produce $^{\bullet}OH$ under visible light, as shown in Fig. 13b.[62,63] The holes consequently move from the VB of TiO_2 to the VB of $CoFe_2O_4$ to react with H_2O/OH^- and produce $^{\circ}OH$.[64,65] This betterment in the photoactivity is related to the p–n junction, and the presence of Ti^{3+}, V_O, $CoFe_2O_4$, and ZnTCPP dye, which increase the photoactivity of TiO_2 in the visible region.

4.3. Comparison with other reported catalysts

The results obtained from the oxidation of alcohols with the ZnTCPP-TiO_2/$CoFe_2O_4$ hybrid were compared with some reported catalysts in other literature studies (Table 6). Considering the used catalyst and alcohol amounts, oxidants, reaction times, and yield percentages, the present method is more suitable. Mainly, catalysts used in most studies took more time for the reaction and a high amount of them was needed. Also, it is noteworthy that due to the powerful magnetic properties of the $CoFe_2O_4$, the ZnTCPP-TiO_2/$CoFe_2O_4$ can be separated from the reaction using a magnet.

Table 6 Comparison of the catalytic efficiency of ZnTCPP-TiO_2/$CoFe_2O_4$ with those of several reported catalysts

No.	Catalyst	Activation method	Oxidant	Yield%	Time (min) of reaction	[Alcohol] (μmol)	[Catalyst] (mg)	Ref.
1	TiO_2/Ti_3C_2	Visible light	O_2	97	300	20	30	66
2	FeOx@N-C/Pd	Visible light	O_2	88	120	200	10	67
3	n-TiO_2-P25@TDI@DES	Visible light	Nitrate	58	1140	150	50	68
4	TiO_2	UV	O_2	52	720	250	40	69
5	Ag_2S-CdS	Visible light	O_2	>99	120	200	10	70
6	NH_2-MIL-125@TAPB-PDA	Visible light	O_2	94.7	1440	200	20	71
7	WO_3ZnO/Fe_3O_4	HP mercury	Air	89	150	1000	10	72
8	0.5 wt% Au-Pd/$ZnIn_2S_4$	Visible light	O_2	90.6	600	250	80	73
9	CQD@IL/WO_4^{2-}	—	H_2O_2	95	120	1000	10	74
10	Zn-TCPP-TiO_2/$CoFe_2O_4$	Visible light	H_2O_2	87	120	100	10	This work

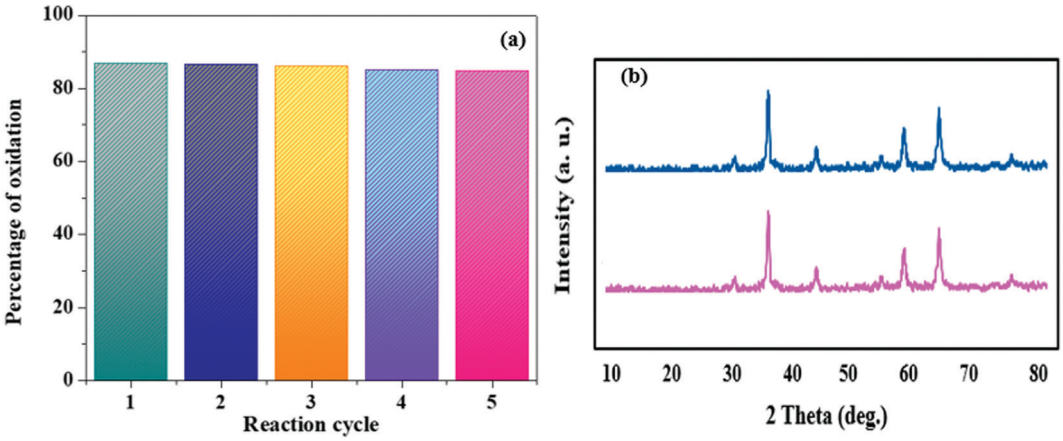

Fig. 14 (a) Recycling of the ZnTCPP-TiO_2/$CoFe_2O_4$ catalyst in the oxidation reaction and (b) XRD patterns of the ZnTCPP-TiO_2/$CoFe_2O_4$ nanohybrid before (blue) and after (pink) recycling.

4.4. Reusability of the ZnTCPP-TiO_2/$CoFe_2O_4$ nanohybrid

The stability of the ZnTCPP-TiO_2/$CoFe_2O_4$ nanohybrid for photocatalytic oxidation was studied *via* the continuous recycling process. Upon completion of the reaction, the photocatalyst was recycled by separating it from the reaction solution using a permanent magnet. The separated catalyst was washed with CH_3CN and dried for the next run. The recovered and reused catalyst shows good activity after 5 recycles (Fig. 14a) with comparable efficiency. As shown in Fig. 14, the photocatalytic performance reduced by 8 percent after 5 cycles which is due to the inevitable loss of the catalyst during the recovery and washing processes for reuse. Only ignorable changes in the yield could be observed which correspond to the XRD patterns of the photocatalyst before and after the reaction in Fig. 14b (blue and pink traces, respectively). Both XRD patterns are the same which confirms the stability of the catalyst owing to the consistency of the ZnTCPP bonding to the surface of the TiO_2/$CoFe_2O_4$. It can be noted that the phase and structure of the ZnTCPP-TiO_2/$CoFe_2O_4$ remained unchanged after the fifth cycle, suggesting that the photocatalyst is robust and stable in the photo-oxidation process.

6. Conclusion

This study demonstrates that the visible light sensitivity of the TiO_2/$CoFe_2O_4$ nanoparticles was enhanced through modification with ZnTCPP. The photocatalytic activity of the ZnTCPP-TiO_2/$CoFe_2O_4$ nanohybrid toward the oxidation of alcohols was compared to those of the TiO_2/$CoFe_2O_4$ and $CoFe_2O_4$ nanoparticles upon exposure to visible light. Using ZnTCPP-TiO_2/$CoFe_2O_4$ as a photocatalyst, the conversion percentage of alcohol to the corresponding aldehyde reached 87%, whereas with $CoFe_2O_4$ and TiO_2/$CoFe_2O_4$, the conversion was less than 39% and 61%, respectively. The higher photocatalytic activity of the ZnTCPP-TiO_2/$CoFe_2O_4$ nanohybrid under visible light was attributed to the presence of Ti^{3+} and V_O as defect sites, as well as strong interactions between ZnTCPP and TiO_2/$CoFe_2O_4$. This new photocatalyst has several advantages over typical nano structured photocatalysts with similar performance, including one-step separation/recycling using a permanent magnet, and stability toward surface site poisoning, without losing efficiency or activity. More generally, the results of this work provide useful guideline principles for the design of complex photocatalysts.

Conflicts of interest

There are no conflicts to declare.

Acknowledgements

The authors gratefully acknowledge the University of Kurdistan, the University of Waterloo, and the Natural Sciences and Engineering Research Council of Canada (RGPIN-2015-04032) for the support provided to this work. The authors thank Dr Paul Stanish for his help with PL measurements, and also Dr Yufeng Zhou and I-Hsuan Yeh for their help with TEM measurements.

References

1 Y. He, Q. He, Z. Liu, O. Wang and M. Guli, *Mater. Technol.*, 2020, **35**, 1–10.
2 H. Cheng, P. Wang, Z. Wang, Y. Liu and B. Huang, *Silver-based visible light-responsive photocatalysts*, 2020, vol. 31.
3 V. KumarGupta, M. LütfiYola, T. Eren, F. Kartal, M. Çağlayan and N. Atar, *J. Mol. Liq.*, 2014, **190**, 133–138.
4 A. M. Balu, B. Baruwati, E. Serrano, J. Cot, J. Garcia-Martinez, R. S. Varma and R. Luque, *Green Chem.*, 2011, **13**, 2750–2758.
5 H. Yang, S. Ji, X. Liu, D. Zhang and D. Shi, *Sci. China: Chem.*, 2014, **57**, 866–872.
6 J. Fan, H. Yang, M. Liu, D. Wu, H. Jiang, X. Zeng, S. Elingarami, Z. Li, S. Li, H. Liu and N. He, *J. Nanosci. Nanotechnol.*, 2015, **15**, 1123–1129.
7 X. Mou, Z. Ali, S. Li and N. He, *J. Nanosci. Nanotechnol.*, 2015, **15**, 54–62.
8 H. Yang, W. Liang, N. He, Y. Deng and Z. Li, *ACS Appl. Mater. Interfaces*, 2014, **7**, 774–781.

9 X. Mou, T. Li, J. Wang, Z. Ali, Y. Zhang, Z. Chen, Y. Deng, S. Li, E. Su, Q. Jia, N. He, J. Ni and D. Cui, *J. Biomed. Nanotechnol.*, 2015, **11**, 2057–2066.
10 P. Liu, W. Qi, Y. Du, Z. Li, J. Wang, J. Bi and W. Wu, *Sci. China: Chem.*, 2014, **57**, 1483–1490.
11 S. Huang, Y. Xu, M. Xie, H. Xu, M. He, J. Xia, L. Huang and H. Li, *Colloids Surf., A*, 2015, **478**, 71–80.
12 N. Chandel, K. Sharma, A. Sudhaik, P. Raizada, A. Hosseini-Bandegharaei, V. K. Thakur and P. Singh, *Arabian J. Chem.*, 2020, **13**, 4324–4340.
13 Q. Sun, S. Wu, K. Li, B. Han, Y. Chen, B. Pang, L. Yu and L. Dong, *Appl. Surf. Sci.*, 2020, **516**, 146142.
14 Q. Tian, W. Wu, L. Sun, S. Yang, M. Lei, J. Zhou, Y. Liu, X. Xiao, F. Ren, C. Jiang and V. A. Roy, *ACS Appl. Mater. Interfaces*, 2014, **6**, 13088–13097.
15 J. Pan, X. Li, Q. Zhaoa and D. Zhang, *RSC Adv.*, 2015, **5**, 51308–51317.
16 S. Afzal, W. A. Daoud and S. J. Langford, *ACS Appl. Mater. Interfaces*, 2013, **5**, 4753–4759.
17 A. Yella, H.-W. Lee, H. N. Tsao, C. Yi, A. K. Chandiran, M. K. Nazeeruddin and E. Wei-Gu, *Science*, 2011, **334**, 629–634.
18 S. Mathew, A. Yella, P. Gao, R. Humphry-Baker, B. F. Curchod, N. Ashari-Astani, I. Tavernelli, U. Rothlisberger, M. K. Nazeeruddin and M. Grätzel, *Nat. Chem.*, 2014, **6**, 242.
19 J. Luo, M. Xu, R. Li, K.-W. Huang, C. Jiang, Q. Qi, W. Zeng, J. Zhang, C. Chi, P. Wang and J. Wu, *J. Am. Chem. Soc.*, 2013, **136**, 265–272.
20 Y. Yuan, H. Lu, Z. Ji, J. Zhong, M. Ding, D. Chen, Y. Li, W. Tu, D. Cao, Z. Yu and Z. Zou, *Chem. Eng. J.*, 2015, **275**, 8–16.
21 M. Ghobadifard, S. Mohebbi and P. V. Radovanovic, *New J. Chem.*, 2020, **44**, 2858–2867.
22 M. Ghobadifard and S. Mohebbi, *New J. Chem.*, 2018, **42**, 9530–9542.
23 M. Ghobadifard, S. Farhadi and S. Mohebbi, *Polyhedron*, 2018, **155**, 66–76.
24 E. Safaei and S. Mohebbi, *J. Mater. Chem. A*, 2016, **4**, 3933–3946.
25 N. G. Singh, K. D. Borah, S. Majumder and J. Bhuyan, *J. Mol. Struct.*, 2020, **1200**, 127116.
26 E. Abroushan, S. Farhadi and A. Zabardasti, *RSC Adv.*, 2017, **7**, 18293–18304.
27 K. Praveena, K. Sadhana, S. Srinath and S. R. Murthy, *J. Phys. Chem. Solids*, 2013, **74**, 1329–1335.
28 A. Manikandan, R. Sridhar, S. Arul Antony and S. Ramakrishna, *J. Mol. Struct.*, 2014, **1076**, 188–200.
29 T. Ali, A. Ahmed, U. Alam, I. Uddin, P. Tripathi and M. Muneer, *Mater. Chem. Phys.*, 2018, **212**, 325–335.
30 P. Şen, C. Hirel, C. Andraud, C. Aronica, Y. Bretonnière, A. Mohammed, H. Ågren, B. Minaev, V. Minaeva, G. Baryshnikov, H.-H. Lee, J. Duboisset and A. Lindgren, *Materials*, 2010, **3**, 4446–4475.
31 G. Granados-Oliveros, E. A. Páez-Mozo, F. M. Ortega, C. Ferronato and J.-M. Chovelon, *Appl. Catal., B*, 2009, **89**, 448–454.
32 J. Rochford, D. Chu, A. Hagfeldt and E. Galoppini, *J. Am. Chem. Soc.*, 2007, **129**, 4655–4665.
33 N. Li, G. Liu, C. Zhen, F. Li, L. Zhang and H. Cheng, *Adv. Funct. Mater.*, 2011, **21**, 1717–1722.
34 J. He, Y. Cheng, T. Wang, D. Feng, L. Zheng, D. Shao, W. Wang, W. Wang, F. Lu, H. Dong, R. Zheng and H. Liu, *Appl. Surf. Sci.*, 2018, **440**, 99–106.
35 J. Li, Q. Pei, R. Wang, Y. Zhou, Z. Zhang, Q. Cao, D. Wang, W. Mi and Y. Du, *ACS Nano*, 2018, **12**, 3351–3359.
36 D. R. Dreyer, S. Park, C. W. Bielawski and R. S. Ruoff, *Chem. Soc. Rev.*, 2010, **39**, 228–240.
37 W. Bian, Z. Yang, P. Strasser and R. Yang, *J. Power Sources*, 2014, **250**, 196–203.
38 I. Luciu, R. Bartali and N. Laidani, *J. Phys. D: Appl. Phys.*, 2012, **45**, 345302.
39 B. Chai, T. Peng, P. Zeng and J. Mao, *J. Mater. Chem.*, 2011, **21**, 14587–14593.
40 B. Bharti, S. Kumar, H.-N. Lee and R. Kumar, *Sci. Rep.*, 2016, **6**, 1–12.
41 P. G. Choi, N. Izu, N. Shirahata and Y. Masuda, *ACS Appl. Nano Mater.*, 2019, **2**, 1820–1827.
42 Q. Zhang, N. Bao, X. Wang, X. Hu, X. Miao, M. Chaker and D. Ma, *Sci. Rep.*, 2016, **6**, 38066.
43 M. Sugawara, *Phys. Rev. B: Condens. Matter Mater. Phys.*, 1995, **51**, 10743.
44 P. Karthik, E. Balaraman and B. Neppolian, *Catal. Sci. Technol.*, 2018, **8**, 3286–3294.
45 N. Ertugay and F. N. Acar, *Appl. Surf. Sci.*, 2014, **318**, 121–126.
46 M. Ghobadifard, S. Farhadi and S. Mohebbi, *Res. Chem. Intermed.*, 2019, **45**, 379–400.
47 G. Tan, L. She, T. Liu, C. Xu, H. Ren and A. Xia, *Appl. Catal., B*, 2017, **207**, 120–133.
48 H. Ji, F. Chang, X. Hu, W. Qin and J. Shen, *Chem. Eng. J.*, 2013, **218**, 183–190.
49 W. Wu, X. Xiao, S. Zhang, F. Ren and C. Jiang, *Nanoscale Res. Lett.*, 2011, **6**, 533.
50 B. Palanisamy, C. M. Babu, B. Sundaravel, S. Anandan and V. Murugesan, *J. Hazard. Mater.*, 2013, **252–253**, 233–242.
51 A. Wisitsoraat, A. Tuantranont, E. Comini, G. Sberveglieri and W. Wlodarski, *Thin Solid Films*, 2009, **517**, 2775–2780.
52 G. H. Jonker, *J. Phys. Chem. Solids*, 1959, **9**, 165–175.
53 S. K. Lakhera, H. Y. Hafeez, P. Veluswamy, V. Ganesh, A. Khan, H. Ikeda and B. Neppolian, *Appl. Surf. Sci.*, 2018, **449**, 790–798.
54 S. K. Lakhera, A. Watts, H. Y. Hafeez and B. Neppolian, *Catal. Today*, 2018, **300**, 58–70.
55 J. Liu, S. Yang, W. Wu, Q. Tian, S. Cui, Z. Dai, F. Ren, X. Xiao and C. Jiang, *ACS Sustainable Chem. Eng.*, 2015, **3**, 2975–2984.
56 Y. H. Hafeez, S. Kumar Lakhera, N. Narayanan, S. Harish, Y. Hayakawa, B.-K. Lee and B. Neppolian, *ACS Omega*, 2019, **4**, 880–891.
57 Y. Zhang, A. M. Schultz, P. A. Salvador and G. S. Rohrer, *J. Mater. Chem.*, 2011, **21**, 4168–4174.
58 Y. Xiang, P. Ju, Y. Wang, Y. Sun, D. Zhang and J. Yu, *Chem. Eng. J.*, 2016, **288**, 264–275.
59 M. Humayun, A. Zada, Z. Li, M. Xie, X. Zhang, Y. Qu, F. Raziq and L. Jing, *Appl. Catal., B*, 2016, **180**, 219–226.
60 B. Qiu, Y. Zhou, Y. Ma, X. Yang, W. Sheng, M. Xing and J. Zhang, *Sci. Rep.*, 2015, **5**, 8591.

61 F. Zuo, D. K. Bozhilov, R. J. Dillon, L. Wang, P. Smith, X. Zhao, P. C. Bardeen and P. P. Feng, *Angew. Chem., Int. Ed.*, 2012, **51**, 6223–6226.
62 H. Huang, K. Xiao, Y. He, T. Zhang, F. Dong, X. Du and Y. Zhang, *Appl. Catal., B*, 2016, **199**, 75–86.
63 H. Huang, X. Han, X. Li, S. Wang, P. K. Chu and Y. Zhang, *ACS Appl. Mater. Interfaces*, 2015, **7**, 482–492.
64 L. Gan, L. Xu and K. Qian, *Mater. Des.*, 2016, **109**, 354–360.
65 P. Zhou, J. Yu and M. Jaroniec, *Adv. Mater.*, 2014, **26**, 4920–4935.
66 X. Bao, H. Li, Z. Wang, F. Tong, M. Liu, Z. Zheng, P. Wang, H. Cheng, Y. Liu, Y. Dai, Y. Fan, Z. Li and B. Huang, *Appl. Catal., B*, 2021, **286**, 119885.
67 M. Dabiri, R. Nikbakht and S. Kazemi Movahed, *Mater. Chem. Phys.*, 2021, **285**, 123908.
68 S. Taghavi, A. Amoozadeh and F. Nemati, *J. Chem. Technol. Biotechnol.*, 2021, **96**, 384–393.
69 A. R. Niaraki, M. R. Saraee, F. Kazemi and B. Kaboudin, *Org. Biomol. Chem.*, 2020, **18**, 2326–2330.
70 Y. Dong, Y. Su, Y. Hu, H. Li and W. Xie, *Small*, 2020, **16**, 2001529.
71 G. Lu, X. Huang, Y. Li, G. Zhao, G. Pang and G. Wang, *J. Energy Chem.*, 2020, **43**, 8–15.
72 B. Li, R. Tayebee, E. Esmaeili, M. S. Namaghi and B. Maleki, *RSC Adv.*, 2020, **10**, 40725–40738.
73 C. Feng, X. Yang, Z. Sun, J. Xue, L. Sun, J. Wang, Z. He and J. Yu, *Appl. Surf. Sci.*, 2020, **501**, 144018.
74 M. Mohammadi, A. Khazaei, A. Rezaei, Z. Huajun and S. Xuwei, *ACS Sustainable Chem. Eng.*, 2019, **7**, 5283–5291.

